Calculated iron $L_{2,3}$ x-ray absorption and x-ray magnetic circular dichroism of spin-crossover Fe(phen)$_2$(NCS)$_2$ molecules adsorbed on a Cu(001) surface

R. Pasquier and M. Alouani ⬤
Université de Strasbourg, Institut de Physique et de Chimie des Matériaux de Strasbourg,
CNRS-UNISTRA UMR 7504, 67034 Strasbourg, France

The projector augmented wave method has been used to compute the iron $L_{2,3}$ edges of x-ray absorption spectra (XAS) and x-ray magnetic circular dichroism (XMCD) of the spin-crossover Fe(phen)$_2$(NCS)$_2$ molecule when adsorbed on Cu(001) surface and in the gas phase, for both the high-spin (HS) and low-spin (LS) states. The electronic structures of both HS and LS states have been calculated using the spin-polarized generalized gradient approximation for the exchange-correlation potential, and the strongly localized iron $3d$ states are described using Dudarev's rotationally invariant formulation of the DFT+U method. It is shown that only the iron all-electron partial waves are necessary to calculate the XAS transition matrix elements in the electric dipole approximation, as the contribution of the pseudo partial waves is compensated by the plane-wave component of the wave function. It is found that the calculated XAS and XMCD with the static core hole or the Slater transition state half hole are in less good agreement with experiment than those using the so called initial state. This disagreement is due to the reduction of the iron spin magnetic moment caused by the static screening of the core hole by the photo-electron. The $L_{2,3}$ XAS formula is found to be directly related to the unoccupied $3d$ density of states (DOS), and hence the symmetry broken e_g and the t_{2g} iron DOS are used to explain the XAS and XMCD results. It is demonstrated that the dependence of the HS XMCD on the direction of incident x-ray circularly polarized light with respect to the magnetization direction can be used to determine the iron octahedron deformation, while the XMCD for various magnetization directions is directly related to the anisotropy of the orbital magnetic moment and the magnetocrystalline energy. The Thole-Carra-Van der Laan XMCD sum rules have been applied to the XMCD $L_{2,3}$ spectra to compute the spin and orbital magnetic moments. It is shown that the magnetic dipole moment T_z is very large due to the strong distortion of the iron octahedron and is necessary for an accurate determination of the sum rule computed spin magnetic moment.

I. INTRODUCTION

Mastering the physics and chemistry of isolated bistable molecules that are adsorbed on surfaces is necessary to further advance information technology as they have potential applications for display devices, data storage, and organic transistors. For example, the spin state of spin-crossover (SCO) molecules can be switched between the low-spin (LS) and high-spin (HS) states by an external perturbation such as a variation in the temperature, light, pressure, magnetic or electric field [1–7]. This artificially triggered $d - d$ electronic transition originates from the redistribution of the transition metal $3d$ electrons between the symmetry broken e_g and t_{2g} orbitals due to the structural deformation of the octahedral transition-metal complex.

X-ray absorption spectroscopy (XAS) and x-ray magnetic circular dichroism (XMCD) techniques have been extensively used to study SCO molecular systems. The absorption spectra of the HS and LS states are quite distinct due to their different magnetic ground-state properties [8–12]. These techniques are therefore powerful characterization tools for studying the spin state of SCO compounds in all magnetic phases. Naturally, such spectra have been computed for the prototype Fe(phen)$_2$(NCS)$_2$ (Fephen) spin-crossover molecule, where phen is the 1,10-phenanthroline, and they are commonly used as a reference by experimentalists working on these systems

[9]. Miyamachi *et al.*, for example, studied the spin-crossover phenomenon in a Fephen system both in the gas phase and adsorbed on a Cu(001) surface along with its XAS and and XMCD [12]. Among other things, a Fano resonance in the conductance at zero-bias was observed only in the HS state. The origin of this anomalous conductance has been arduous to elucidate due to the subtle electronic coupling between the surface and the complex, and it has led to an extensive body of work [13].

From a fundamental perspective, the transition from the HS to LS in Fe(II) complexes involves the spin transition $(t_{2g})^{3\uparrow}(e_g)^{2\uparrow}(t_{2g})^{1\downarrow} \rightarrow (t_{2g})^{3\uparrow}(t_{2g})^{3\downarrow}(e_g)^0$ (see Ref. [14]). This spin transition stabilizes the low-spin state because of the full occupation of the low-lying symmetry broken t_{2g} energy levels. It is therefore interesting to compute the LS and HS XAS $L_{2,3}$ edges from first principles and compare them directly to experiment to validate this spin transition. To this end, we have calculated the x-ray absorption spectra and XMCD of the Fephen molecule both on the gas phase and adsorbed on a Cu(001) surface in the electric dipole approximation and have compared our findings to experiment [12]. We have shown, in particular, that the XAS and XMCD calculations including the static core hole are in a worse agreement with experiment than the calculations using the ground state. This fact remains true even when using the Slater transition rule,

where only a half hole is used in the $2p$ core states [15,16]. This disagreement is explained below in terms of the reduction of spin moment caused by the additional screening of the core hole by the photoelectron. In addition, we have demonstrated that the dependance of the XMCD signal on the direction of incident circularly polarized light can be used to determine the deformation of the iron octahedron, and the XMCD for various magnetization orientations gives the anisotropy of the orbital magnetic moment, which is related to the magnetocrystalline energy (MCA). Those findings were not investigated in Ref. [12] but are very useful for the characterization of SCO molecules adsorbed on a metallic substrate.

To understand the distinct characteristics associated with absorption spectra of the HS and LS, we have first shown that the XAS is related to the $3d$ density of states and the XAS results can therefore be explained in terms of the density of states of the $3d$ electrons. We have therefore compared the symmetry broken parent e_g and t_{2g} density of states to the calculated XAS results [17]. We have also tested the validity of the so-called XMCD sum rules for molecular systems and shown that it is necessary to take into account the contribution of the magnetic dipole operator T_z to obtain spin magnetic moments in agreement with those obtained from the electronic structure calculation or experiment. Finally, we have derived the plane-wave contribution to the x-ray electronic transition matrix elements within the projected augmented plane wave (PAW) method [18] and have shown that it has a negligible effect on the XAS and XMCD.

This paper is organized as follows: In the second section, we provide a brief description of our method of calculation and implementation of the XAS and the XMCD in VASP and show that the dependence of the XMCD on the direction of the incident circularly polarized x-ray beam is directly related to the distortion of the iron octahedron. In addition, using the XMCD sum rules we show that the XMCD for different magnetization directions can be used to determine the anisotropy of the orbital magnetic moment. In a third section, we present our results for the XAS and XMCD at the iron $L_{2,3}$ edges for both the gas phase and the molecule adsorbed on a Cu(001) surface and compare them to the available experimental data and show that the calculation without static core hole is in better agreement with experiment. We then give an interpretation of the HS and LS XAS and XMCD in terms of symmetry broken e_g and t_{2g} density of states. At the end of this section, we demonstrate how to utilize the XMCD sum rules to compute the spin and orbital magnetic moments as well as the importance of the magnetic dipole moment for the determination of the spin magnetic moment. The derivation of the plane-wave contribution to the x-ray matrix elements, the implementation of the magnetic dipole moment in the VASP package, as well as the approximation of the XAS by weighted partial density of states of the conduction electrons are provided in the appendices.

II. COMPUTATIONAL METHOD

A. Computational details

The electronic structure is computed using VASP (Vienna *Ab initio* Simulation) package [19–23], which implements

the Kohn-Sham density functional theory (DFT) within the PAW method [18]. The spin-polarized generalized gradient approximation (GGA) with the Perdew-Burke-Ernzerhof (PBE) functional [24] is employed to describe the exchange-correlation potential, whereas the van der Waals interaction, which is relevant mostly between the surface and the molecule, is taken into account using the semi-empirical Grimme approximation at the DFT-D2 level [25]. Note that we have attempted to use the more accurate DFT-D3 and DFT-D4 methods, but we have encountered convergence issues. The strongly localized iron $3d$ states are described using Dudarev's rotationally invariant formulation of Liechtenstein's DFT+U method [26,27]. The value of the effective Hubbard parameter is $U - J = 2.1$ eV, which accurately reflects the energy difference between the two spin states of Fe(II) [28]. The total energy is converged to 10^{-5} eV and the plane-wave cutoff is set at 500 eV. The ionic force relaxation threshold is set at 5×10^{-2} eV/Å in each direction. We have used a supercell with dimensions $20.4 \times 20.4 \times 30$ Å^3. The surface is simulated using a $8 \times 8 \times 3$ stack of copper oriented along the (001) direction and contains 192 atoms. The Fermi energy has been calculated using a Gaussian smearing with a width of 0.1 eV. This entropy has been removed from the computed total energy. The calculations are carried at the Γ point only given the large dimensions of the supercell.

B. X-ray absorption and XMCD

One can define the x-ray absorption cross section with polarization μ in a general way using Fermi's golden rule [29],

$$\sigma^{\mu}(\omega) = \frac{4\pi\alpha\hbar}{m_e^2\omega} \sum_{if} |\langle f|p_{\mu}|i\rangle|^2 \delta(\hbar\omega - \epsilon_f + \epsilon_i). \quad (1)$$

Here, α is the fine-structure constant, m_e is the electron mass, i and f stand respectively for the core states and the conduction states, and their energies ϵ_i and ϵ_f). Here $p_{\mu} = -i\hbar\nabla_{\mu}$ is the projection of the momentum operator on the $\{\mu = -1, 0, 1\}$ polarization direction. These directions, along with the corresponding cross section, are defined as

$$\sigma^{\mu=\pm} : p_{\mu=\pm} = \frac{\mp 1}{\sqrt{2}}(p_x \pm ip_y),$$

$$\sigma^{\mu=0} : p_{\mu=0} = p_z. \quad (2)$$

There are several ways to calculate the x-ray absorption cross section, ranging from the analytical evaluation of transition matrix elements [30] to core-hole [31], or ligand field DFT methods [32]. In this study, our approach is based on the PAW method within the DFT calculations to compute these matrix elements, and it has been already used to compute the K and $L_{2,3}$ edges in iron to achieve quantitative agreement with experimental data [33]. Here, we extend our method by including the plane-wave contribution and thus enabling the computation of the XMCD spectra for any direction of the magnetization and any direction of the incident circularly polarized x ray. We have also determined the XAS in terms of the partial density of states of the probed atom. This will be used later to analyze the different features in the XAS in terms of the symmetry broken e_g and t_{2g} density of states of

the ideal octahedron. Note that in this formalism, its straightforward to include the effect of a static core hole or to use the Slater transition rule [15,16], where only one half core state is included. However, the static core hole usually only slightly improves the K-edge spectrum, but it seldom leads to improved $L_{2,3}$ edges compared to calculations with the initial state [34]. Indeed, we will show below that the initial state calculation agrees better with experiment than calculations using a static full core hole or Slater's half hole.

Within PAW [18], the core states are considered frozen and kept unchanged in the pseudopotential files, and they are usually fully relativistic $|J, M\rangle$, i.e., solutions to the Dirac equation [35]. This means that we need to work in a $|JMLS\rangle$ coupled basis set,

$$
\begin{aligned}
|i\rangle = |J, M\rangle &= \sum_{m',s} \langle \ell', m', 1/2, s | J, M \rangle |\ell', m', 1/2, s\rangle \\
&= \sum_{m',s} C^{J,M}_{\ell',m',1/2,s} |\ell', m', 1/2, s\rangle,
\end{aligned} \tag{3}
$$

where ℓ, m, and s the usual angular momentum and spin quantum numbers, the $C^{J,M}_{\ell',m',1/2,s}$ are the usual Clebsch-Gordan coefficients and $\ell' = 1$ for the $L_{2,3}$ edges. It should be noted that we disregard the contribution of the minor part of the Dirac bispinor when computing the matrix elements because the conduction states are scalar relativistic and the small component contribution is negligible. The conduction states are the computed Kohn-Sham orbitals $|n, \mathbf{k}, s\rangle$, which can be written in the PAW method as

$$
\begin{aligned}
|f\rangle = |n, \mathbf{k}, s\rangle = \widetilde{|n, \mathbf{k}, s\rangle} &+ \sum_{p,\ell,m} \widetilde{P}^{n,\mathbf{k},s}_{p,\ell,m} (|p, \ell, m, s\rangle \\
&- \widetilde{|p, \ell, m, s\rangle}),
\end{aligned} \tag{4}
$$

where n is the band index, $\mathbf{k}$ the wave vector, and s the spin index. $\widetilde{P}^{n,\mathbf{k},s}_{p,\ell,m}$ is the projection value of the pseudo Kohn-Sham wave functions on the PAW projector functions (for more details see Ref. [18]). Here p is used for multiple projector functions to improve the atomic basis set. Usually p is limited to one or two projector functions per angular momentum ℓ.

It should be noted that our implementation can include only the static core-hole effects using a supercell geometry, unlike other PAW implementations, such as the Taillefumier *et al.* method [36] where a continued fraction formulation was used to compute the K-edge x-ray absorption near-edge structures in presence of a core hole. However, our calculations do not include multiplet structures and dynamical core-hole screening. Although this appears to be a drastic approximation, we will show that our implementation is sufficient to obtain qualitative agreement with experiment. The $\widetilde{|n, \mathbf{k}, s\rangle}$ are the so-called pseudo wave functions associated with the pseudo-partial waves $\widetilde{|p, \ell, m, s\rangle}$, whereas the $|p, \ell, m, s\rangle$ are the all electron partial waves. The pseudo and plane-wave contributions will be shown to be negligible as the $3d$ electrons of iron are strongly localized within the augmentation region, and these corrections are hence extremely small up to several dozens of eV above the Fermi level. They are therefore only relevant for EXAFS, which is not the subject of this paper. This naturally leads us to limit the calculation to the

relevant photoelectron energy range when not including the plane-wave contribution. These partial waves are indexed by p the projector index, and ℓ, m, and s the usual angular momentum and spin quantum numbers, with $P^{n,\mathbf{k},s}_{p,\ell,m}$ the associated projection value of the Kohn-Sham pseudo wave functions,

$$
P^{n,\mathbf{k},s}_{p,\ell,m} = \langle g_{p,\ell,m,s} | \widetilde{n, \mathbf{k}, s} \rangle, \tag{5}
$$

where $g_{p,\ell,m,s}$ are the usual PAW projector functions. Note that VASP uses cubic harmonics $\mathcal{Y}^m_\ell$, whereas the formula is computed for spherical harmonics Y^m_ℓ. We should then transform the projections back into the spherical harmonics basis when doing the actual computation by using the usual unitary transformation U from cubic to spherical harmonics. We can show that it amounts in writing the projections as $P^{n,\mathbf{k},s}_p = U^{-1} * \widetilde{P}^{n,\mathbf{k},s}_p$, where $\widetilde{P}^{n,\mathbf{k},s}_p$ represents the vector of the cubic projections, as given by Eq. (4) that are computed by VASP.

Using these formulas together with the golden rule, we can find

$$
\begin{aligned}
\sigma^\mu(\omega) = \frac{4\pi\alpha\hbar}{m_e^2\omega} \sum_{M,n,\mathbf{k},s} &\left| \sum_{p,\ell,m,m'} C^{J,M}_{\ell',m',1/2,s} \langle p, \ell, m | p_\mu | \ell', m' \rangle \right. \\
&\left. \times P^{*n,\mathbf{k},s}_{p,\ell,m} \right|^2 \delta(\hbar\omega - \epsilon_{n\mathbf{k}s} + \epsilon_{JM}),
\end{aligned} \tag{6}
$$

where we have used the fact that the spin is conserved by the momentum operator. The $\epsilon_{n\mathbf{k}s}$ and ϵ_{JM} are respectively the Kohn-Sham eigenvalues and the relativistic core energies. Note that VASP does not compute the spin-orbit splitting between the $(J - 1/2)$ and $(J + 1/2)$ core states, and we have therefore taken this splitting from the result of a relativistic all electron atomic program calculation [37]. This also implies that the spectra $\sigma^\mu(\omega)$ are J dependent, although this will be kept implicit in our notations.

Using Wigner-Eckart's theorem [38,39], one can then show that

$$
\langle p, \ell, m | p_\mu | \ell', m' \rangle = \frac{C^{\ell,m}_{\ell',m',1,\mu}}{C^{\ell,0}_{\ell',0,1,0}} \langle p, \ell, 0 | p_0 | \ell', 0 \rangle. \tag{7}
$$

We therefore recover the so-called dipolar selection rules: $\ell = \ell' \pm 1$ and $m = \mu + m'$. Using angular momentum algebra [39], we have the following closed formula that will be used to compute the reduced matrix element for each projector p:

$$
\begin{aligned}
\langle p, \ell, 0 | \nabla_0 | \ell', 0 \rangle = &\, \delta_{\ell,\ell'+1} \frac{\ell}{\sqrt{(2\ell-1)(2\ell+1)}} \left[(\phi_{p,\ell} | \partial_r | \phi^c_{\ell'}) \right. \\
&\left. - (\ell-1)(\phi_{p,\ell} | r^{-1} | \phi^c_{\ell'}) \right] \\
&+ \delta_{\ell,\ell'-1} \frac{\ell+1}{\sqrt{(2\ell+1)(2\ell+3)}} \left[(\phi_{p,\ell} | \partial_r | \phi^c_{\ell'}) \right. \\
&\left. + (\ell+2)(\phi_{p,\ell} | r^{-1} | \phi^c_{\ell'}) \right],
\end{aligned} \tag{8}
$$

where we introduced the radial functions associated with the core ϕ^c or the conduction states ϕ, along with the radial integration $(\phi_{p,\ell} | r^\alpha | \phi^c_{\ell'}) = \int dr \phi_{p,\ell}(r) r^{\alpha+2} \phi^c_{\ell'}(r)$. Note that for most weakly relativistic systems such that $\alpha^2 Z^2 \ll 1$ (including iron, where $\alpha^2 Z^2 \approx 0.03$), the fine structure corrections to the radial eigenfunctions are very small [40] and consequently
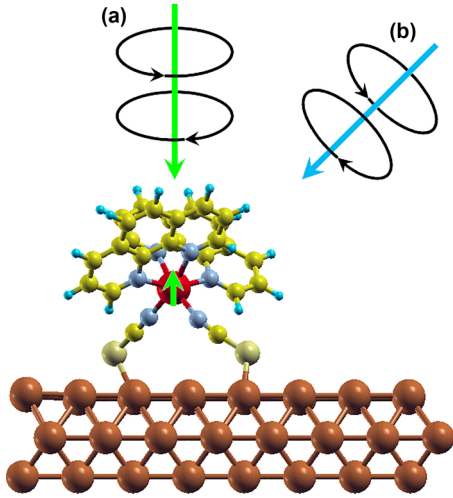
FIG. 1. Fephen molecule on top of the Cu(001) surface. The direction of the incident circularly polarized light is along the z direction (A) and along $\vartheta = \varphi = \pi/4$ (B). The spin magnetic moment direction is set along the z direction, perpendicular to the Cu(001) surface, when the spin-orbit coupling is included.
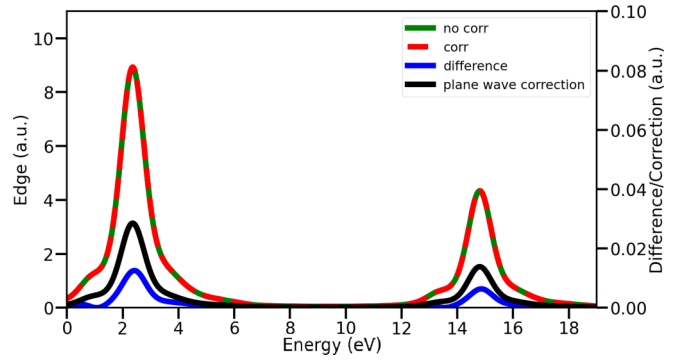

FIG. 2. Comparison between the all electron partial wave (green) and the full PAW wave function (red) calculated iron $L_{2,3}$ XAS spectra for the LS state. The negligible difference (blue) of the spectra as well as the plane-wave contribution to the XAS (black) are shown on the right scale.

one can safely use nonrelativistic radial wave functions for the core states. However, VASP allows us to compute the relativistic radial wave functions by solving Dirac's align, so we will use them.

To conclude, in the momentum representation, the following expression for the absorption spectrum can be shown,

$$\sigma^{\mu}(\omega) = \frac{4\pi\alpha\hbar^3}{m_e^2\omega} \sum_{M,n,k,s} \left| \sum_{p,\ell,m,m'} C^{J,M}_{\ell',m',1/2,s} \frac{C^{\ell,m}_{\ell',m',1,\mu}}{C^{\ell,0}_{\ell',0,1,0}} \right.$$
$$\left. \times \langle p, \ell, 0 | \nabla_0 | \ell', 0 \rangle P^{*n,\mathbf{k},s}_{p,\ell,m} \right|^2 \delta(\hbar\omega - \epsilon_{n\mathbf{k}s} + \epsilon_{JM}).$$
$$(9)$$

The polarization is defined as in Eq. (2), and the XAS and XMCD corresponding respectively to the $\sigma_{XAS} = \frac{1}{3}(\sigma^0 + \sigma^- + \sigma^+)$ and $\sigma_{XMCD} = \sigma^+ - \sigma^-$ spectra are computed using Eq. (9). The matrix elements $\langle p, \ell, 0 | \nabla_0 | \ell', 0 \rangle$ are computed using Eq. (8), and the radial integrations are cut at the augmentation radius for consistency. However, given the low symmetry of the molecule under study, it is important to note that the dependence of the XMCD signal on the direction of the incident circularly polarized light is a signature of the distortion of the iron octahedron. Here we have used a global coordinates system (O, x, y, z) and have assumed that the direction of incident light is given by the two spherical angles (ϑ, φ). We can therefore write the cross section σ_{XMCD} for any incident light direction specified by ϑ, φ as shown in Fig. 1. The figure shows also that the spin quantization direction is fixed along a given direction, as it would be done experimentally with a magnetic field. Here we take the (001) direction as a reference. It will be shown later that this direction corresponds to the lowest total energy when the spin-orbit coupling is included. We need therefore to rotate the matrix elements from the local frame of reference (O, x', y', z'), where the z' direction is along the incident light, to the global frame. This

transformation is provided by the direction cosine rotation matrix,

$$R(u, v, w) = R_{z'}(\varphi) \cdot R_{y'}(\vartheta)$$
$$= \begin{pmatrix} \frac{uw}{\sqrt{1-w^2}} & -\frac{v}{\sqrt{1-w^2}} & u \\ \frac{vw}{\sqrt{1-w^2}} & \frac{u}{\sqrt{1-w^2}} & v \\ -\sqrt{1-w^2} & 0 & w \end{pmatrix}, \quad (10)$$

where the direction cosines are defined as $u = x/r$, $v = y/r$, and $w = z/r$, where $r = \sqrt{x^2 + y^2 + z^2}$. We can show that the XMCD signal for any direction (ϑ, φ) is given by

$$\sigma_{XMCD}(\omega) = u\sigma^{yz}(\omega) + v\sigma^{zx}(\omega) + w\sigma^{xy}(\omega), \quad (11)$$

and where $\sigma^{\mu\nu}$ is given by

$$\sigma^{\mu\nu}(\omega) = \frac{4\pi\alpha\hbar}{m_e^2\omega} \sum_{if} \Im(\langle f | p_\mu | i \rangle \langle i | p_\nu | f \rangle) \delta(\hbar\omega - \epsilon_f + \epsilon_i). \quad (12)$$

Here $\Im$ is the imaginary part, and $\mu, \nu = x$, y, or z.

We have demonstrated that the plane-wave contribution to the x-ray absorption matrix elements compensates almost perfectly the pseudo partial wave contribution. The derivation of the matrix element is shown in Appendix B. As shown in Fig. 2, the effects of the plane-wave contribution to the $L_{2,3}$ XAS and XMCD are extremely small. This was to be expected as we are only interested in a limited energy range above the Fermi energy for the $L_{2,3}$ edges, that are primarily associated with the $3d$ part of the eigenfunctions localized within the augmentation region. To utilize the so called XMCD sum rules [41–43] to compute the spin and orbital moments, we need to know to evaluate carefully the number of electrons in the valence states n_e. In principle as we are truncating the plane-wave component of the wave function, and we are therefore restricting ourselves to the augmentation region contribution to the density of states, which will not integrate to the theoretical values of $n_e = 6$ below the Fermi energy or $n_e = 10$ over the entire energy range. In practice, doing so yields less accurate values for the sum rules than the theoretical value of $n_h = 4$ that we will therefore use. We will also show in the results that we need to evaluate the magnetic
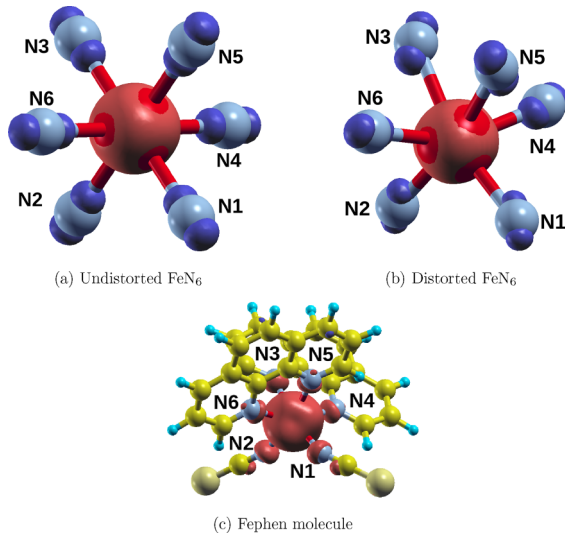
(a) Undistorted FeN$_6$

(b) Distorted FeN$_6$

(c) Fephen molecule

FIG. 3. Comparison of the high-spin isosurface of the magnetization density of undistorted (a) and distorted (b) FeN$_6$ cluster with that of the Fephen in (c) gas phase and (d) adsorbed on the Cu(001) surface. The red color represents the positive magnetization (majority spin up), and blue the negative magnetization (minority spin down). For all cases, the isosurface is taken to be $\pm 0.025 \mu_B$ per unit cell.

dipole contribution $\langle T_z \rangle$ to obtain accurate values of the spin and orbital magnetic moments. The $\langle T_z \rangle$ contribution will be directly evaluated in DFT using the formula derived in the Appendix.

III. RESULTS AND DISCUSSION

To illustrate the effect of various atoms of the molecule on the electronic structure of the iron atom, and therefore on its high-spin state XAS absorption and XMCD, we depict in Fig. 3 the magnetization isosurface at $\pm 0.025 \mu_B$ per unit cell for the undistorted (top left) and distorted (top right) (as in the molecule on the copper surface) FeN$_6$ cluster together with that of the molecule in the gas phase (bottom left) and that on the substrate (bottom right). Due to the direct hybridization of the p orbitals of nitrogen with those of the iron site, the magnetic moments of all the N atoms are oriented opposite to that of the iron site. This does not apply to the case of the free FeN$_6$ octahedron (for more details see Supplemental Material Figs. S1 and S2 and the effect on the iron density of states Figs. S3 and S4 [44]). This is because the nitrogen atoms are chemically bonded to the carbon atoms of the phenanthroline. Table I shows the iron number of electrons and magnetic moment in FeN$_6$ cluster and in the molecule. It is clear from the table that the distortions have only a slight impact on the electronic distribution of the iron atom, but as shown later, the XMCD is considerably modified. As a result, new σ^{xz} and σ^{zy} signals appear. This is also true for the free molecule as compared to the molecule on the Cu(001) substrate, as the Fe $-$ N bond lengths of the free molecule deviate differently from the average bond length than for the adsorbed molecule. We have found that the relative root mean-square deviation (RMSD) percentage, which is defined as the RMSD divided by the average bond length, for the HS free molecule is 5.1%

TABLE I. Iron site number of electrons and spin magnetic moments in units of μ_B per s, p, and d orbitals for ideal and distorted FeN$_6$ cluster together with the Fephen molecule in the gas phase and the one adsorbed on Cu(001) surface.

System	n_s	n_p	n_d	m_s (μ_B)	m_p (μ_B)	m_d (μ_B)
Ideal FeN$_6$	0.370	0.422	5.838	0.039	−0.029	3.237
Distorted FeN$_6$	0.386	0.460	5.877	0.030	−0.004	2.996
Fe in Fephen	0.327	0.451	5.982	0.017	0.026	3.696
Fe in Fephen/Cu(001)	0.304	0.407	6.007	0.017	0.022	3.635

whereas it is only 3.6% for the HS adsorbed molecule, and where the average bond length are respectively 2.15 Å and 2.17 Å. Note that for the low spin the respective relative RMSDs are about the same, 1.3% and 1.6%, with an almost equal average bond length of 1.96 Å.

The XAS and XMCD $L_{2,3}$ spectra were computed for the Fephen molecule up to 6.5 eV above the Fermi energy. The calculations are done using the relaxed atomic positions of the molecule. The root mean square deviation from the experimental atomic positions for the free molecule is about 0.2 Å for the HS and 0.1 Å for the LS. The difference between the XAS spectra calculated with the experimental positions and the calculated ones is negligible. The L_2 and L_3 edges are split by the relativistic $p_{1/2} - p_{3/2}$ spin-orbit energy, which we have found to be 12.45 eV using an atomic all-electron relativistic program [37]. The program also produced a $p_{3/2}$ energy shift of 0.66 eV towards higher energies for the spin-polarized state compared to the non-spin-polarized one. The $L_{2,3}$ edges are broadened by a Gaussian function of full width of 0.25 eV and a Lorentzian function of 0.5 eV, leading to a Voigt profile with a broadening ≈ 0.6 eV, in agreement with experimental results [45]. To determine the effect of the static core hole on the XAS, we have performed a calculation including a static core hole in the core $2p$ states, and also a half hole according to the Slater transition rule. We have compared in Fig. 4 the calculation of XAS and XMCD using the so-called initial state, where no core hole is included, with the calculation using a full core hole and that using a Slater half hole. We observe that the structures in the LS XAS are shifted linearly towards lower energies by 2 eV for the full core hole and 1 eV for the half hole. This shift corresponds to the screening of the core hole by the additional photo-electron that remains on the iron site. The linear reduction of the peak intensity also corresponds to the overall reduction in the number of unoccupied states in the $3d$ density of states of iron. The situation is similar for the HS XAS, but it is less pronounced than for the LS case, and we observe also a clear reduction of the peak intensities.

The reduction of the peak intensity of the first structure is clearly in disagreement with experiment as it will be shown in Fig. 5. The calculated spin magnetic moment is also drastically reduced from 3.696 μ_B without core hole to 3.06 μ_B with a half core hole and 2.452 μ_B for a full self-consistent core hole. This shows the limitation of XAS calculations using a static core hole. Unfortunately, calculations beyond a static core hole, such as using the Bethe-Salpeter equation to
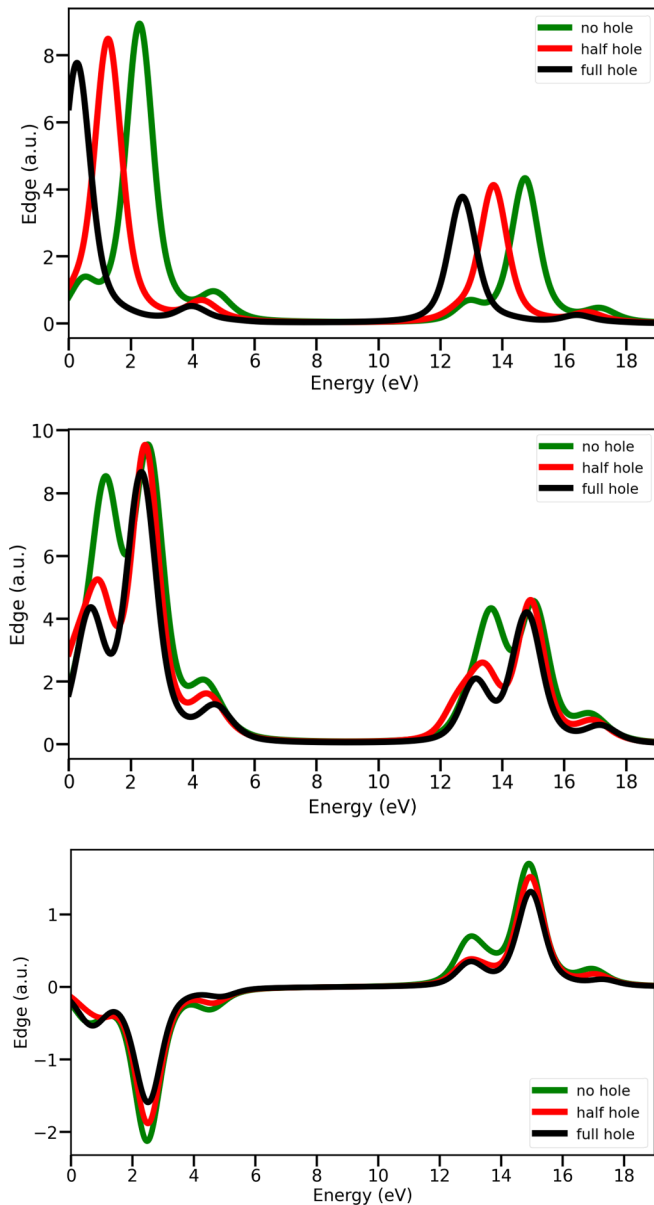
FIG. 4. $L_{2,3}$ XAS for the Fephen molecule without core hole (green), with the Slater transition rule half hole (red) and the full hole (black), both for the HS (top) and LS (middle) and the corresponding HS XMCD spectra (bottom).
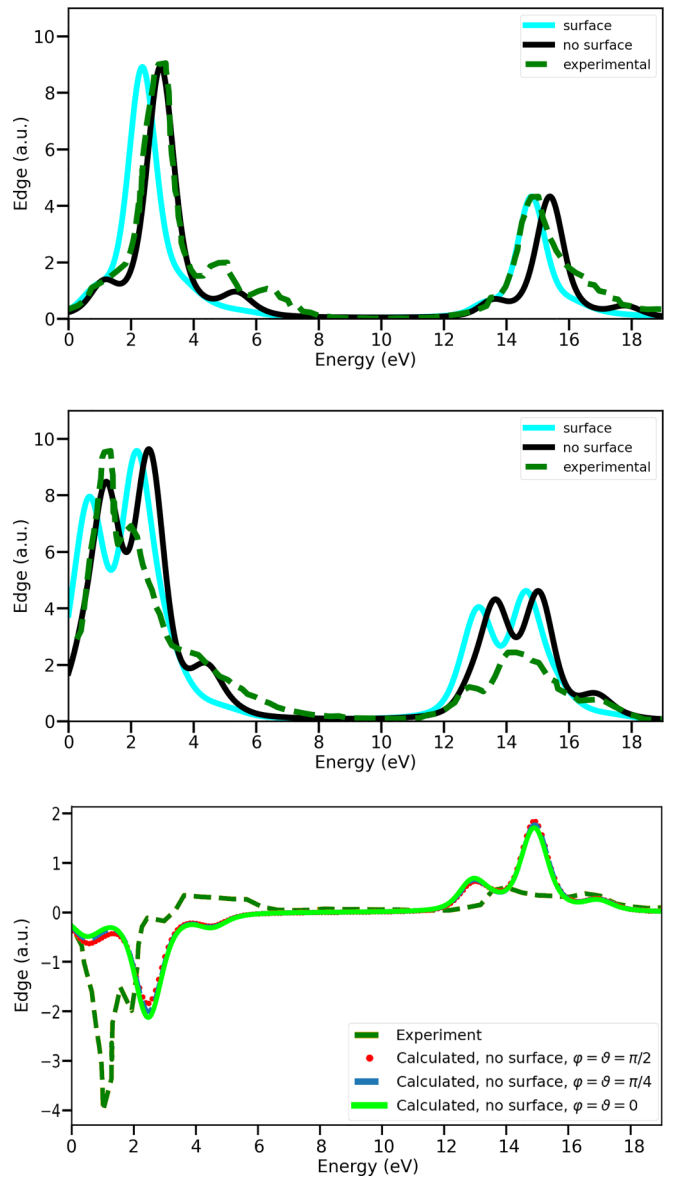

FIG. 5. $L_{2,3}$ XAS for the Fephen molecule in the LS state (top), HS state (second), and HS XMCD for the free molecule (third) compared with the experimental results of Ref. [12] for the gas phase. The XMCD is calculated for the magnetic moment aligned along the (001) direction (green), the (111) (dot-dashed blue), and (010) (dashed red).

compute the electron-hole interaction, are not feasible for such a large system because of the prohibitive computer cost [46,47] and it is the reason that the formalism have been used only for materials with only few atoms per unit cell.

Since calculations including a static core hole deviate more from the experimental XAS spectra of Miyamachi *et al.* [12], we have shown in Fig. 5 only the calculated x-ray XAS and XMCD using the initial state and have compared our results to the experimental spectra. We have adjusted the energy reference by shifting the theoretical LS spectrum relative to the HS one by our computed value of 0.66 eV. We have then plotted the experimental LS spectrum for the gas phase by adjusting the well-defined L_3 peak as a reference point, and the HS spectrum being then automatically obtained and

compared to the experimental one. We can see that the calculation reproduces the $L_{2,3}$ edges in the LS state, but as expected the multiplets, which are not taken into account in the calculation, are not reproduced. It is interesting to note that the spectrum for the molecule on the surface is similar to that of the gas phase, apart from the structure at about 5 eV, which is strongly reduced. The two spectra for the gas phase and for the adsorbed molecule are shifted by the difference of their respective Fermi levels. In the case of the HS state, we note a less accurate agreement between the theoretical and experimental results as the experimental peaks are slightly shifted and have different intensities for the L_2 and L_3 edges. These differences might be dependent on

the dynamics of the core hole [48], although we still have a qualitative agreement.

For the XMCD, we have made calculations for three alignments of the magnetic moment. The first for the moment along the (001) easy axis, and the second and the third for the moment along the (111) and (010) directions. Note that the magnetic moment direction has a negligible effect on the total XAS. These XMCD results for various magnetization directions will be used later to determine the orbital magnetic moment anisotropy by means of the XMCD sum rules. As it can be seen from Fig. 5 the agreement with the experimental data is only qualitative. This is expected, as the XMCD simulation is notoriously complex. It relies on the difference between two relatively close spectra for left and right circular polarizations, and it is therefore extremely sensitive to numerical errors and approximations. Indeed, one can easily observe that the XMCD spectrum vanishes exactly if spin-orbit coupling is not taken into account as both spin channels will then couple identically with the photon helicity, and therefore both left and right polarizations give the same results. As such, the value of the orbital moment is strongly dependent on the accuracy of the spin-orbit treatment, which, therefore, constitutes an important source of error as it is numerically very difficult to compute accurately for such a large molecule.

So far we have only compared our calculation to the experimental results of the gas phase Fephen molecule. However, Miyamachi *et al.* [12] have also measured the XAS of two layers of Fephen molecules adsorbed on the Cu(001) surface and found that the $L_{2,3}$ XAS corresponds to a mixture of 46% of HS and 54% of LS signals. The LS and HS mixture is found by fitting the XAS of the two layers of Fephen molecules adsorbed on Cu(001) using a linear combination of the powder XAS spectra of the LS and HS. It is surprising to notice that the XAS for powder provided a good fit to the XAS of the molecule adsorbed on the Cu(001) surface. To shed some light on the experimental data, we have also made a fit of the experimental XAS by combining our LS and HS XAS of the molecule adsorbed on the surface. We have proceeded as in the experiment by linearly combining our spectra: $r\sigma^{\mathrm{LS}}(\omega + \Delta) + (1 - r)\sigma^{\mathrm{HS}}(\omega + \Delta)$, where $\Delta = 0.7\,\mathrm{eV}$ is the energy difference between the corresponding peak positions of the LS XAS of the gas phase and that of the molecule adsorbed on the Cu(001) surface, and r is the amount of LS proportion.

As shown in Fig. 6 (top) the amount r of the LS is found to be 37% for the best agreement with experiment, whereas experimentalists have found a value of 54%. We have also shown the spectrum corresponding to the experimental LS amount of 54%, which was not very different from that of the optimal r amount. As stated above the agreement of the experimental XAS spectra of the gas phase molecule with the one where the molecule is adsorbed on the surface is surprising. As shown by our calculation, the Fermi level of the molecule adsorbed on the surface is shifted by 1.2 eV towards higher energy with respect to the gas phase. It is therefore unlikely that the XAS experimental peak positions of the free molecule and the one adsorbed on the surface are not shifted with respect to one another, but it is also possible that a significant amount of the molecules is not adsorbed on the surface as the Fephen had a
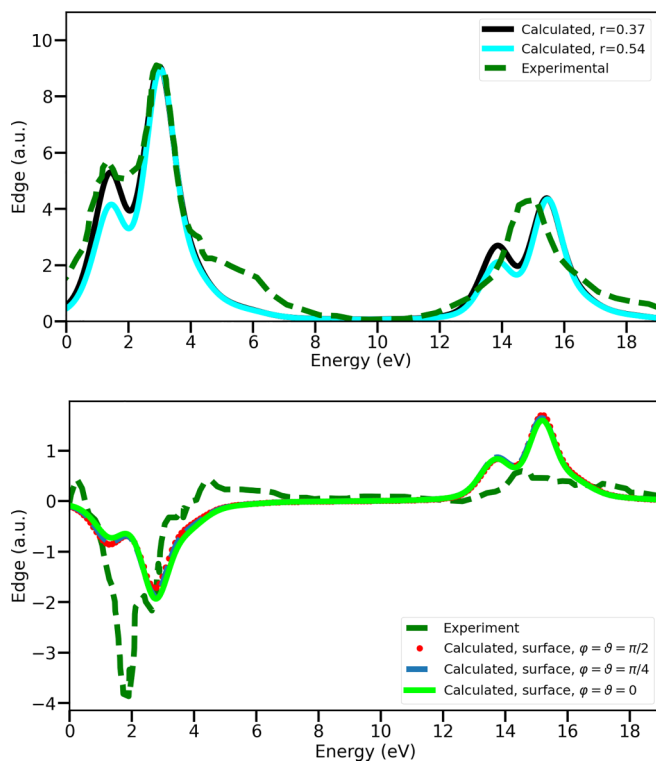

FIG. 6. Linear combination of LS (37% black, 54% blue) and HS (63% black, 46% blue) $L_{2,3}$ XAS for the Fephen molecule on Cu(001) compared with the experimental results of Ref. [12]. The bottom figure shows the XMCD at the $L_{2,3}$ of iron for the molecule adsorbed on Cu(001) compared to the experimental results of [12]. The XMCD is calculated for the magnetic moment aligned along the (001) direction (green), the (111) (dot-dashed blue), and (010) (dashed red).

2 ML thickness. This claim could be experimentally verified and explored, e.g., by measuring the spectra of one Fephen monolayer or less on the surface. Figure 6 (bottom) shows also the calculated and measured XMCD. The agreement with experiment is similar to that for the molecule on the gas phase.

As explained in the method of calculation, we have found that the dependance of the XMCD on the direction of the incident light can be used to provide the deformation of the iron octahedron, whereas the dependance on the magnetization direction produces the anisotropy of the orbital magnetic moment. To support our idea, we have depicted in Fig. 7 the $\sigma^{\mu\nu}$ components as given by Eq. (12) for the $L_{2,3}$ iron atom in the molecule on Cu(001) and for the iron atom in the distorted and undistorted FeN$_6$ octahedra. For the undistorted tetrahedron, the σ^{yz} and σ^{zx} are exactly zero due to symmetry and the code also produces zero, whereas these two components of the σ tensor do not vanish for the distorted octahedron, as shown in Fig. 7 (bottom). It is clear that if we set the direction of the circularly polarized light along (010) or (100) direction, while keeping the magnetization along the (001) direction, we will observe only σ^{yz} or σ^{zx} as shown by Eq. (12). It is therefore interesting to emphasize that this kind of experiment will directly give the effect of the octahedron distortion on the XMCD signal. One can set a database of XMCD spectra for a direction where the the XMCD should
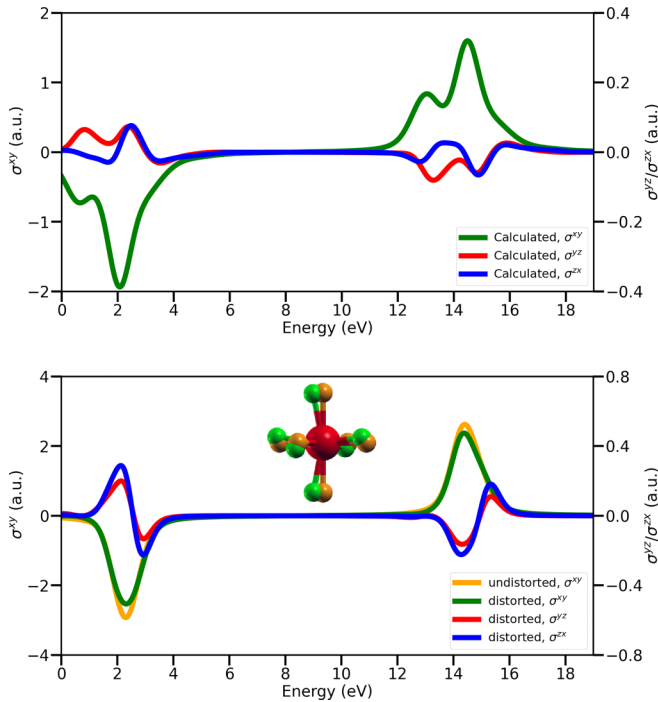
FIG. 7. Calculated $\sigma^{\mu\nu}$ [see Eq. (12)] for the HS Fephen molecule (top) when the magnetic moment is aligned along the (001) axis and for perfect and deformed FeN_6 octahedron (bottom). σ^{yz} and σ^{zx} are strictly zero by symmetry for the undistorted octahedron (not shown). The scale of σ^{yz} and σ^{zx} is on the right. The inset shows the the deformation of the octahedron (nitrogen atoms in green) as in the molecule case compared to the nondeformed one (Nitrogen in orange).

be zero for a perfect octahedron and machine learning can be used to predict the octahedron distortion of SCO molecules adsorbed on metallic surfaces. These theoretical predictions are interesting and need future experimental confirmation, as most available results yet deal with the crystalline phase, which is clearly isotropic.

To describe further the distortion from the octahedral symmetry on the x-ray absorption we have first analyzed the deformation of the octahedron for both the gas phase molecule and the one on the surface. The method used to compute the deformation is well described in Appendix A. We have calculated the distortion of the octahedron from an ideal one and found that in the HS the octahedron of the free molecule is more deformed than that of the adsorbed one (see Supplemental Material Fig. S5 for further details on the effect of the octahedron distortion on the iron $L_{2,3}$ [44]). Indeed the cost function L defined in Appendix A has a value of 0.016 in the gas phase but only 0.011 in for adsorbed molecule as shown in Table IV of Appendix A. This is also compatible with the relative RMSD of the bond length discussed previously. We have therefore analyzed the anisotropy of the x-ray absorption by computing $\Delta\sigma/\sigma^0$, where $\Delta\sigma = (\sigma^+ + \sigma^-)/2 - \sigma^0$, as shown in Fig. 8. Note that this anisotropy should be zero for a perfect octahedron and a nonzero value gives us the degree of deformation of the octahedron. As is expected, the figure shows that this anisotropy is strong, and it is much larger for the free molecule
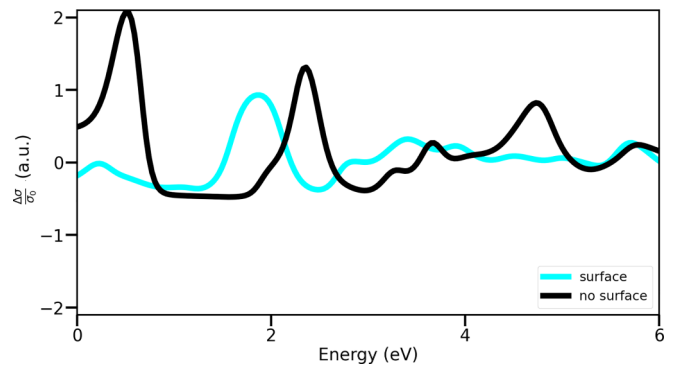

FIG. 8. Calculated XAS anisotropy $\Delta\sigma/\sigma^0$, where $\Delta\sigma = (\sigma^+ + \sigma^-)/2 - \sigma^0$ for the molecule in the gas phase (black) and adsorbed on Cu(001) surface (blue).

compared to the adsorbed molecule. This is unexpected as we might assume that the surface will deform further the octahedron. In fact the opposite happens when the molecule is adsorbed on the surface because the octahedral angle between the NCS groups is reduced from 102.4 to 96.3 degrees. This reduction is certainly due to the lattice spacing between the surface copper atoms, which constrains the sulfur-sulfur distance (see Fig. 1 as the sulfur of the NCS group is known to establish strong bonds with transition metals.

To understand the structures in the XAS, we have compared them in Fig. 9 with the spin-polarized symmetry broken e_g and t_{2g} representations of the iron site density of states (for more details see Supplemental Material Figs. S3 and S4 [44]). As expected from the d^6 electronic configuration of the ground state, the density of states shows that the primary states contributing to the LS XAS signal are from the unoccupied parent e_g states. As for the HS XAS, the main contribution are from the minority spin parent splitted t_{2g} and e_g states. These splittings of the e_g and t_{2g} states are due to both the strong crystal-field effect and the distorted iron octahedron [14]. This interpretation is compatible with the structural and electronic structure transition from the HS to LS, which involves the spin transition $(t_{2g})^{3\uparrow}(e_g)^{2\uparrow}(t_{2g})^{1\downarrow} \rightarrow (t_{2g})^{3\uparrow}(t_{2g})^{3\downarrow}(e_g)^0$ as shown in Ref. [14]. The figure also shows that the states contributing to the HS XMCD spectrum are naturally the same as those for the HS XAS. It is evident that the sum rules should be vanishing in the LS state and the numerical calculation concurs with this analytical result. However, this is not the case in the HS state, for which we get the results shown in Table II. These results are obtained from the XMCD spectra presented in Fig. 5 when the polarization is along the (001), (111), and (010) directions. We did not evaluate the sum rules for the experimental spectrum because we encountered normalization issues, which lead to nonphysical values (e.g., m_ℓ has a computed value of several μ_B). Table II also shows that the magnetocrystalline energy ΔE is lowest when the magnetic moment is oriented along the (001) direction and the hard axis is aligned with the (010) direction. This energy ΔE is equivalent to a blocking temperature of 22 K, which is very low considering the superparamagnetic aspect of the molecular crystal. We can make several interesting observations:

TABLE II. Magnetocrystalline anisotropy energy ΔE in meV, direct calculation of magnetic dipole (T_z), spin moment (m_s), and orbital moment (m_ℓ) compared to those obtained using the XMCD sum rules (in units of Bohr magneton μ_B) for the iron site of the SCO Fephen in the HS state for various directions of the iron magnetic moment. The hard axis total energy is -1045.48985 eV.

Magnetization direction	ΔE (meV)	T_z (μ_B)	m_ℓ (μ_B)		m_s (μ_B)	
			Direct	Sum rule	Direct	Sum rule
(001)	−1.9	−0.101	0.180	0.154	3.635	3.731
(111)	−0.98	−0.092	0.106	0.092	3.637	3.735
(010)	0	−0.092	0.006	0.006	3.635	3.734

(i) The magnetic dipole tensor is nonvanishing, and its value is non-negligible as it makes up for roughly 10% of the magnetic moment contribution. One could have expected this, as it was shown that this operator takes a finite value for ideal Fe^{+2} octahedral complexes in the HS state when spin-orbit coupling is taken into account [49]. However, as we show in the Appendices, relativistic corrections are not the dominant contribution to the value of this tensor in our case as they are almost negligible. Instead, it appears that the likely origin of this behavior is imperfect octahedral geometry of the high-spin complexes, which significantly lifts the degeneracy of the parent t_{2g} and e_g states, and as such removes the symmetries that nullify the value of T_z.

(ii) The orbital momentum sum rule yields a slightly underestimated value of $0.154\mu_B$ compared to the directly calculated value of $0.180\mu_B$ when the magnetization is oriented along the easy axis (001). As the accuracy of this value depends directly on the integral of the XMCD signal, such an agreement is quite surprising as one would expect a worse accordance especially given the relatively poor agreement between the theoretical and experimental spectra that demonstrated the limitation of the model. We also note that the sum rules are an approximate theoretical results, and as such the range of their validity has been debated [48,50]. Nevertheless, according to Schwitalla and Ebert [48], they should be decently accurate for Fe^{2+} compounds. It should also be emphasized that the integrated spectra over the relevant energy range, used for the sum rules, are in general less sensitive to the details of their structures and shapes [50].

(iii) The spin-moment sum rule appears to yield a quite accurate value of $3.731\mu_B$ compared to direct calculated value of $3.635\mu_B$. We can appreciate here the importance of the magnetic dipole correction as shown in Table III, as without it the sum rule would only yield a moment of $3.377\mu_B$, which

TABLE III. Value of T_z in the molecular systems in the HS and LS state (in μ_B).

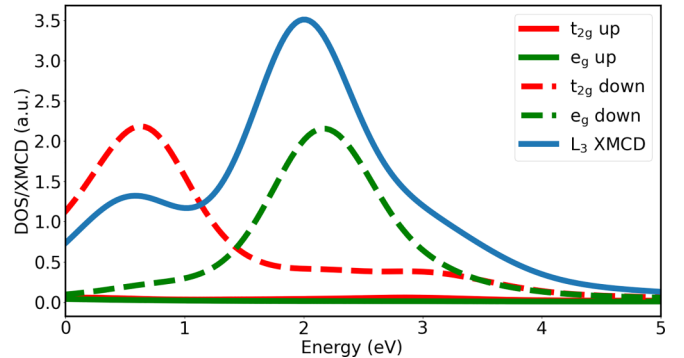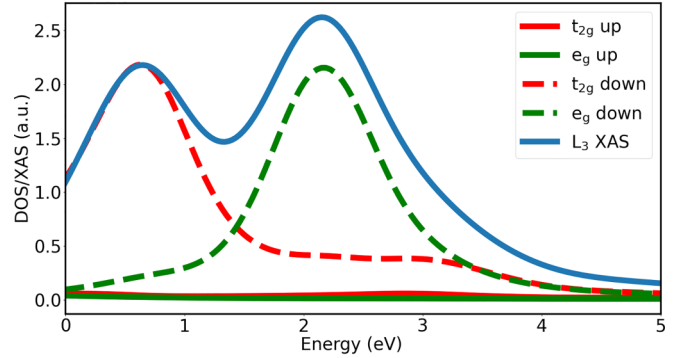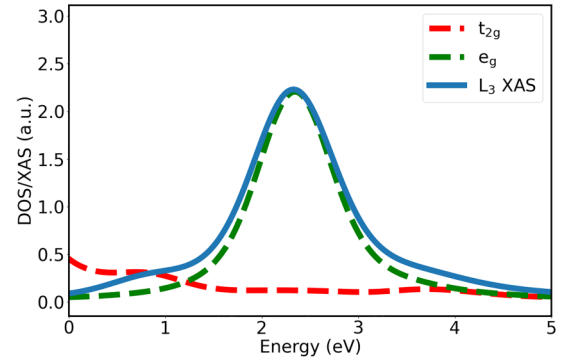| Molecule	NSOC	SOC
LS (surface/gas)	0	0
HS (surface)	−0.091	−0.101
HS (gas phase)	−0.150	−0.161

FIG. 9. The iron site spin-polarized symmetry broken e_g and t_{2g} decomposed unoccupied density of states compared to the calculated XAS L_3 spectrum for both LS (top) and HS (middle) and to HS XMCD (bottom). Note the XMCD sign is flipped for an easy comparison.

is still within an acceptable range from the expected value. It appears, therefore, that this spin sum rule is less sensitive to inaccuracies in the XMCD spectrum than the orbital moment sum rule. This is not surprising, as the orbital moment is much smaller compared to the spin magnetic moment and is consequently much more prone to errors.

IV. CONCLUSIONS

Our implementation of the XAS and XMCD spectra within VASP has been used to compute the $L_{2,3}$ edges for both the low-spin and high-spin iron site within a SCO Fephen molecule in the gas phase and adsorbed on a copper surface. We have found that the plane-wave contribution to the x-ray matrix elements within the electric dipole approximation are

small and fully compensated by the pseudopartial contribution to the PAW wave function within the XAS energy range.

The calculated XAS and XMCD results are in qualitative agreement with the available experimental results, although with relative intensity issues in the HS state that underscore the importance of multiplet and dynamics of the core-hole effects for a comprehensive understanding of the spectrum. We have found that the simple static core hole or the Slater transition rule half hole did not improve the agreement with experiment due to reduction of the iron magnetic moment caused by the additional screening of the core hole by the photo-electron. The calculation using the initial state produced therefore the best agreement with experiment and the overall features in both the HS and LS spectra are understood in terms of the parent symmetry broken e_g and t_{2g} iron $3d$ DOS. The measured XAS of Fephen on the surface is found indeed to be a mixture of HS and LS in agreement with experiment. We have also found that the dependence of the XMCD signal on the direction of incident x-ray circularly polarized light can be used to directly measure the deformation in the iron octahedron. As discussed above, one could attempt to establish a database for the σ^{yz} and σ^{zx} XMCD directions, which are zeros for a perfect octahedron, and use machine learning to determine directly the octahedron distortion of the SCO molecules.

We have also shown that the XMCD for different magnetization directions is related to the anisotropy of the iron orbital magnetic moment. As a result, the sum rules yield the correct orbital and spin magnetic moments as compared to direct calculations for different orientations of the spin magnetic moment, as long as one takes into account the contribution of the magnetic dipole moment originating from the geometrical deformation of the iron site octahedron in the HS state. These theoretical predictions await future experimental confirmation.

APPENDIX A: THE MAGNETIC DIPOLE OPERATOR

The magnetic dipole tensor can be defined as

$$\hat{\mathbf{T}} = \hat{\mathbf{S}} - 3\hat{\mathbf{r}}(\hat{\mathbf{r}} \cdot \hat{\mathbf{S}})/|r|^2, \tag{A1}$$

where $\hat{\mathbf{S}}$ is the vector spin operator, and $\hat{\mathbf{r}}$ is the position operator. With a spin quantization axis along z, the magnetic dipole operator can then be written as

$$\hat{\mathbf{T}} = \hat{S}_z - 3\hat{\mathbf{r}}(\hat{r}_z\hat{S}_z)/|r|^2. \tag{A2}$$

As stated earlier, one can show that the sum rules normally include a $\langle\hat{T}_z\rangle$ contribution in the valence shell of angular

momentum ℓ. We will now explicitly compute the value of this tensor using DFT in order to justify our approximation. We start by writing the $\hat{T}_z$ tensor as

$$\hat{T}_z = \hat{S}_z\big(1 - 3\hat{r}_z^2/|r|^2\big) = \hat{S}_z\big(1 - 4\pi\big(\hat{Y}_1^0\big)^2\big), \tag{A3}$$

where Y_1^0 is the spherical tensor operator associated to the spherical harmonic Y_1^0. Then, its mean value in some shell of electrons with angular momentum ℓ can be evaluated in the PAW method as

$$\langle\hat{T}_z\rangle = \sum_{n,\mathbf{k},s} f_{n,\mathbf{k},s}\langle n, \mathbf{k}, s|\hat{T}_z|n, \mathbf{k}, s\rangle$$

$$= \sum_{n,\mathbf{k},s} f_{n,\mathbf{k},s} \sum_{\substack{p,m \\ p',m'}} P^{*n,\mathbf{k},s}_{p',\ell,m'} P^{n,\mathbf{k},s}_{p,\ell,m}\langle p', \ell, m', s|\hat{T}_z|p, \ell, m, s\rangle, \tag{A4}$$

where we once again disregard the plane-wave contribution as we are only interested in the augmentation region in this calculation, and we have introduced the Fermi occupations $f_{n,\mathbf{k},s}$ so that the sum naturally only runs over the occupied states. Using its definition, the matrix elements of $\hat{T}_z$ in the partial wave basis can be written as

$$\langle p', \ell, m', s|\hat{T}_z|p, \ell, m, s\rangle$$
$$= \langle p', \ell, m', s|\hat{S}_z\big(1 - 3\hat{r}_z^2/|r|^2\big)|p, \ell, m, s\rangle$$
$$= \langle p', \ell, m', s|\hat{S}_z\big(1 - 4\pi\big(\hat{Y}_1^0\big)^2\big)|p, \ell, m, s\rangle$$
$$= m_s\big(\langle p', \ell, m, s|p, \ell, m, s\rangle\delta_{m,m'}$$
$$- 4\pi\langle p', \ell, m', s|\big(\hat{Y}_1^0\big)^2|p, \ell, m, s\rangle\big), \tag{A5}$$

where m_s is the magnetic moment. Using the definition of the spherical harmonics [39], one can show that

$$\big(\hat{Y}_1^0\big)^2 = \sqrt{\frac{1}{4\pi}}\hat{Y}_0^0 + \sqrt{\frac{1}{5\pi}}\hat{Y}_2^0. \tag{A6}$$

This leads to the following:

$$\langle p', \ell, m', s|\hat{T}_z|p, \ell, m, s\rangle$$
$$= -4\sqrt{\frac{\pi}{5}}m_s\langle p', \ell, m', s|\big(\hat{Y}_2^0\big)|p, \ell, m, s\rangle. \tag{A7}$$

The matrix element involves an integral over three spherical harmonics Y_2^0, Y_l^m, and $Y_l^{m'}$. This is known in the literature as a Gaunt coefficient [39], and can be shown to be equal to

$$\langle p', \ell, m', s|\big(\hat{Y}_2^0\big)|p, \ell, m, s\rangle$$
$$= \sqrt{\frac{5}{4\pi}}C^{\ell,m'}_{2,0,\ell,m}C^{\ell,0}_{2,0,\ell,0}(p', \ell|p, \ell), \tag{A8}$$

where the $(p', \ell|p, \ell)$ are the radial integration as defined in Eq. (8). By angular selection rules, we directly have that $m' = m$. Therefore, we obtain that

$$\langle\hat{T}_z\rangle = -2\sum_{n,\mathbf{k},s} f_{n,\mathbf{k},s} \sum_{\substack{p,m \\ p'}} P^{*n,\mathbf{k},s}_{p',\ell,m} P^{n,\mathbf{k},s}_{p,\ell,m} m_s C^{\ell,m}_{2,0,\ell,m} C^{\ell,0}_{2,0,\ell,0}$$
$$\times (p', \ell|p, \ell), \tag{A9}$$

which we implemented directly in VASP.

Note that this contribution always vanishes for a perfect O_h symmetry complex of a $3d$ transition metal without spin-orbit

coupling. In order to demonstrate this, we first note that in that case the magnetic dipole moment can be rewritten as

$$\langle \hat{T}_z \rangle = -4\sqrt{\frac{\pi}{5}} \sum_i m_{s,i} \langle i|(\hat{Y}_2^0)|i\rangle \qquad (A10)$$

$$= -2\sqrt{\frac{\pi}{5}} \sum_{u,d} \left(\langle u|(\hat{Y}_2^0)|u\rangle - \langle d|(\hat{Y}_2^0)|d\rangle \right), \qquad (A11)$$

where the index i runs over all the electrons of the ground state, and u, d runs over the up and down populations respectively. For a d^6 Fe^{2+} complex, we now need to consider the ground-state configuration in both spin states:

(a) In the LS state, the ground state corresponds to a closed t_{2g} subshell. In that case, the magnetic dipole operator is trivially vanishing as the two spin contributions that are summed over are the same up to the spin sign.

(b) In the HS state, the ground state can be constructed by half-filling all five d orbitals with the same spin direction, then filling with an equal probability one of the three t_{2g} orbitals with an electron of opposite spin. Sum rules over the Clebsch-Gordan coefficients can be used to show that

$$\sum_m C^{2,m}_{2,0,2,m} = 0$$

$$\times 2C^{2,-1}_{2,0,2,-1} + 2C^{2,1}_{2,0,2,1} + C^{2,2}_{2,0,2,2} + C^{2,-2}_{2,0,2,-2} = 0.$$
$$(A12)$$

Using the definition of the d orbitals and Eq. (A8), it can easily be seen that the majority spin contribution to the magnetic dipole operator is proportional to the first line, whereas the minority spin is proportional to the second line. As such, the magnetic dipole tensor vanishes exactly in this case.

When the spin-orbit interaction is taken into account, the moment still vanishes in the LS state as the two spinor directions are effectively degenerate in that case and we can therefore use a very similar reasoning than in the nonrelativistic case. The case of the HS state is much more complex, and it can be shown that the magnetic dipole tensor takes a non-vanishing value for certain ground-state geometries, including the d^6 geometry of Fe^{2+} [49]. With this in mind, we computed the value of the magnetic dipole moment in our molecules with (SOC) and without (NSOC) the spin orbit (see Table III). As expected, the magnetic dipole operator vanishes in the low-spin state. For the high-spin state, we immediately note that the moment is superior in the gas phase than on the surface, but most importantly that the operator does not vanish even without spin orbit, and the spin orbit contribution is minimal. To rationalize this apparent contradiction, we need to recall that our previous reasoning was only valid for a perfect octahedral geometry, and that the deformation of a real complex is often non-negligible especially in the HS state. Distortion is known to play a noticeable effect on the features of x-ray absorption spectra (see for example Ref. [51]), and therefore it is of no surprise that it should influence the value of T_z (this was already noted, but not shown explicitly, in [30]). Informally, the distortion breaks the ideal symmetry between the d states that is observed in Eq. (A10), and as consequence the sum rules of Eq. (A12) are no longer applicable. Instead, each state is now a mixture weighted by the PAW projections such as in Eq. (A9), and there is no *a priori* reason for the said

sum to vanish when both spin directions are not degenerate such as in the HS state, even in the absence of SOC. In order to give a better illustration of this phenomenon, we will quantify the "amount" of deformation of these systems away from their ideal geometry. We need first to optimally rotate and rescale our system before comparing it to a reference geometry. This is the essence of the so-called extended orthogonal Procrustes algorithm [52]. As a short summary, assume a set of points **u** and a reference set of points **v** (the molecular octahedral coordinates and an ideal octahedron coordinates respectively in our case). An obvious way of defining a "distance" to quantitatively compare these structures is to carry a root median square displacement calculation (RMSD) between these two structures, taking into account the fact that both systems need to be properly rescaled together to have an accurate comparison. Then, we can recast the associated least-square deviation problem as a search for the ideal rotation **R** and scale factor c between **u** and **v**, so that we can write the cost function associated to this RMSD calculation as

$$L(\theta, \Phi) = \frac{1}{2}||\mathbf{v} - c\mathbf{R}(\theta, \Phi)\mathbf{u}||^2,$$

that needs to be minimized over the set of angular variables (θ, Φ) and c. For the rotation part, the solution can be found ([52]) by computing the singular value decomposition of the covariance matrix $H = \mathbf{u^T v}$,

$$\mathbf{H} = \mathbf{U\Sigma V^T} \rightarrow \mathbf{R} = \mathbf{V\Sigma' U^T},$$

where $\mathbf{\Sigma'}$ is a $3x3$ diagonal matrix with diagonal elements $d_1 = 1$, $d_2 = 1$, and $d_3 = \text{sign}(\det(\mathbf{VU^T}))$, which is used to enforce the positive definiteness of the determinant of the rotation matrix, so that we always have a proper transformation. For the scale factor, using the definition of the matrix norm $||A|| = \text{Tr}(A^T A)$ in the previous formula for the RMSD cost function, one can show ([52]) that the minimization yields the following result:

$$c = \frac{\text{Tr}(\mathbf{u^T R^T v})}{\text{Tr}(\mathbf{u^T u})}. \qquad (A13)$$

Applying these to our case, we can obtain a quantitative estimate of the deviation of the molecular geometries from the ideal octahedral geometry. We also add a deviation to an ideal tetrahedral geometry by comparing it to an imperfect tetrahedron using the four shortest ligand bonds in our molecular octahedron (as the average bond length in a tetrahedral complex is shorter than for an octahedral complex).

We can see that the octahedral RMSD is an order of magnitude higher in the high-spin state than the low-spin state, and the same applies to the ratio between the octahedral and tetrahedral RMSD as shown in Table IV. As such, not only is the geometry more strongly deformed in the high-spin state than in the low-spin states, the non-negligible ratio between the octahedral and tetrahedral RMSD in the HS state shows that the absolute deformation away from the ideal case is sizeable. Besides, the deformation in the HS state is clearly larger in the gas phase than when the molecule is adsorbed on the surface. It is therefore of no surprise that the magnetic dipole operator does not vanish in this case, even without several other spin transition compounds, and the same behavior is observed each time. Also, early results show that the moment is a very approximately increasing function of the RMSD.

TABLE IV. Value of the loss function in the molecular systems (in Å^2) with respect to an ideal octahedral and tetrahedral geometry, and ratio between the two values

	HS (gas phase)	HS (surface)	LS (gas phase)	LS (surface)
Octahedral loss	0.016	0.011	0.002	0.002
Tetrahedral loss	0.044	0.048	0.082	0.147
Ratio Oct/Tet	0.363	0.229	0.024	0.014

However, this approach is quite rough as it "averages" over all the angular and length distortions and therefore it will not be able to discriminate between the finer details that characterize distortion, and as a consequence the exact dependence of the magnetic dipole moment with the value of the RMSD is highly nontrivial.

APPENDIX B: PLANE-WAVE CONTRIBUTION TO XAS MATRIX ELEMENTS

The total plane-wave contribution can be split into two parts: the pseudo partial wave contribution $|\widetilde{p, \ell, m}\rangle$ and the actual plane-wave part $|\widetilde{n, \mathbf{k}, s}\rangle$, so the Golden Rule could be written as

$$
\begin{aligned}
\sigma^\mu(\omega) = \frac{4\pi\alpha\hbar}{m_e^2\omega} \sum_{M,n,\mathbf{k},s} \Bigg| & \sum_{p,\ell,m,m'} C^{J,M}_{\ell',m',1/2,s} \\
& \times (\langle p, \ell, m| - \langle \widetilde{p, \ell, m}|) p_\mu |\ell', m'\rangle P^{*n,\mathbf{k},s}_{p,\ell,m} \\
& + \sum_{m'} C^{J,M}_{\ell',m',1/2,s} \langle \widetilde{n, \mathbf{k}, s}|p_\mu|\ell', m'\rangle \Bigg|^2 \\
& \times \delta(\hbar\omega - \epsilon_{n\mathbf{k}s} + \epsilon_{JM}). \quad \text{(B1)}
\end{aligned}
$$

Obviously, the calculation of the pseudo partial wave contribution is identical to that of the previously calculated partial wave part. On the other hand, the plane-wave contribution is more involved. One starts by the plane-wave expansion,

$$
\begin{aligned}
\langle r|\widetilde{n, \mathbf{k}, s}\rangle &= \frac{1}{\sqrt{\Omega}} \sum_\mathbf{G} c^{n,\mathbf{k},s}_\mathbf{G} \langle r|\mathbf{k}+\mathbf{G}\rangle \\
&= \frac{1}{\sqrt{\Omega}} \sum_\mathbf{G} c^{n,\mathbf{k},s}_\mathbf{G} e^{i(\mathbf{k}+\mathbf{G})(\mathbf{r}'+\tau_\alpha)}. \quad \text{(B2)}
\end{aligned}
$$

where $\mathbf{r} = \mathbf{r}' + \tau_\alpha$ is the global electron position, split into the nucleus position τ_α and the local position (with respect to the nucleus) $\mathbf{r}'$. Note that the $|\mathbf{k}+\mathbf{G}\rangle$ are the eigenfunctions of the momentum operator p_μ: $p_\mu|\mathbf{k}+\mathbf{G}\rangle = (k_\mu + G_\mu)|\mathbf{k}+\mathbf{G}\rangle$. The plane-wave expansion is normalized by the system volume Ω. In this local frame, one can then carry a partial wave expansion of the plane wave,

$$
e^{i(\mathbf{k}+\mathbf{G})\cdot\mathbf{r}'} = 4\pi \sum_{\ell,m} i^\ell j_\ell(|(\mathbf{k}+\mathbf{G})||\mathbf{r}'|) Y^{m*}_\ell(\widehat{\mathbf{k}+\mathbf{G}}) Y^m_\ell(\widehat{\mathbf{r}'}),
$$
$$(B3)$$

where the j_ℓ are the usual spherical Bessel functions. Therefore, we can write the following:

$$
\begin{aligned}
& \langle \widetilde{n, \mathbf{k}, s}|p_\mu|\ell', m'\rangle \\
&= \frac{4\pi}{\sqrt{\Omega}} \sum_{\mathbf{G},\ell,m} i^{-\ell} \left(c^{n,\mathbf{k},s}_\mathbf{G}(k_\mu + G_\mu)\right)^\star Y^m_\ell(\widehat{\mathbf{k}+\mathbf{G}}) e^{-i(\mathbf{k}+\mathbf{G})\cdot\tau_\alpha} \\
&\quad \times \int dr\, r^2 j_\ell(|(\mathbf{k}+\mathbf{G})|r)\phi_{\ell'}(r) \int d\widehat{\mathbf{r}} Y^{m'}_{\ell'}(\widehat{\mathbf{r}}) Y^{m*}_\ell(\widehat{\mathbf{r}}).
\end{aligned}
$$
$$(B4)$$

Then, using the orthogonality of the spherical harmonics, we get that

$$
\begin{aligned}
\langle \widetilde{n, \mathbf{k}, s}|p_\mu|\ell', m'\rangle &= \frac{4\pi}{\sqrt{\Omega}} \sum_\mathbf{G} i^{-\ell'} \left(c^{n,\mathbf{k},s}_\mathbf{G}(k_\mu + G_\mu)\right)^* Y^{m'}_{\ell'} \\
&\quad \times (\widehat{\mathbf{k}+\mathbf{G}}) e^{-i(\mathbf{k}+\mathbf{G})\cdot\tau_\alpha} \\
&\quad \times \int dr\, r^2 j_{\ell'}(|(\mathbf{k}+\mathbf{G})|r)\phi_{\ell'}(r). \quad \text{(B5)}
\end{aligned}
$$

This contribution can then be added to the absorption cross section using formula (B1).

APPENDIX C: RELATION BETWEEN XAS AND LOCAL DOS

It is interesting to note that the XAS can be shown to be directly related to the iron 3d DOS, as noted for example in [53]. In our formulation, the relation takes a very simple form. First, we will need to use the position representation of the transition operator. Using the Schröedinger equation, one can easily show that the Hamiltonian H and the position operator r_μ follow the commutation relation $[r_\mu, H] = i\hbar p_\mu/m_e$. This allows us to rewrite the cross section as

$$
\sigma^\mu(\omega) = 4\pi\alpha\hbar\omega \sum_{M,n,\mathbf{k},s} \left| \sum_{m'} C^{J,M}_{\ell',m',1/2,s} \langle n, \mathbf{k}, s|r_\mu|\ell', m'\rangle \right|^2 \delta(\hbar\omega - \epsilon_{n\mathbf{k}s} + \epsilon_J).
$$

Note that we used here the fine-structure degeneracy of the $\epsilon_{JM} = \epsilon_J$ over the set of M that was not relevant thus far for this study. We can then expand the squared norm as

$$
\sigma^\mu(\omega) = 4\pi\alpha\hbar\omega \sum_{\substack{M,m',m'' \\ n,\mathbf{k},s}} C^{J,M}_{\ell',m',1/2,s} C^{J,M}_{\ell',m'',1/2,s} \langle n, \mathbf{k}, s|r_\mu|\ell', m'\rangle \langle \ell', m''|r_\mu|n, \mathbf{k}, s\rangle
$$

$$
\delta(\hbar\omega - \epsilon_{n\mathbf{k}s} + \epsilon_J) = 4\pi\alpha \sum_{\substack{M,m',m'' \\ n,\mathbf{k},s}} (\epsilon_{n\mathbf{k}s} - \epsilon_J) C^{J,M}_{\ell',m',1/2,s} C^{J,M}_{\ell',m'',1/2,s} \langle n, \mathbf{k}, s|r_\mu|\ell', m'\rangle \langle \ell', m''|r_\mu|n, \mathbf{k}, s\rangle \delta(\hbar\omega - \epsilon_{n\mathbf{k}s} + \epsilon_J), \quad \text{(C1)}
$$

where we rewrote $\hbar\omega$ as $\epsilon_{nk s} - \epsilon_J$ thanks to the delta function as we will need it for a following approximation. We will sum over the $\ell + 1/2$ edge $\sigma^\mu_{\ell+1/2}(\omega)$ and $\ell - 1/2$ edge $\sigma^\mu_{\ell-1/2}(\omega)$. To do so, we first need to shift them together as both spectra have different core energy references. We arbitrarily take the $\ell + 1/2$ edge, and shift it by $\Delta\omega_J = (\epsilon_{\ell-1/2} - \epsilon_{\ell+1/2})/\hbar$. Doing so yields

$$\sum_J \sigma^\mu_J(\omega) \approx 4\pi\alpha \sum_{\substack{J,M,m',m'' \\ n,\mathbf{k},s}} (\epsilon_{nk s} - \epsilon_{\ell-1/2}) C^{J,M}_{\ell',m',1/2,s} C^{J,M}_{\ell',m'',1/2,s} \langle n, \mathbf{k}, s | r_\mu | \ell', m' \rangle \langle \ell', m'' r_\mu | n, \mathbf{k}, s | \rangle \delta(\hbar\omega - \epsilon_{nk s} + \epsilon_{\ell-1/2}),\quad \text{(C2)}$$

where we have neglected the variation of ϵ_J with respect to $\epsilon_{nk s}$, because the core energies are located at several thousands of eV below the Fermi energy compared to our EXAFS range of a few hundreds of eV at the highest, and as such we will now write $\epsilon_{\ell-1/2} = \epsilon_C$. Now, we can use the orthogonality property of the Clebsch-Gordan coefficients.

$$\sum_{J,M} C^{J,M}_{\ell',m',1/2,s} C^{J,M}_{\ell',m'',1/2,s} = \delta_{m',m''},$$

$$\sum_{m_1,m_2} C^{J,,M}_{\ell_1,m_1,\ell_2,m_2} C^{J',M'}_{\ell_1,m_1,\ell_2,m_2} = \delta_{J,J'}\delta_{M,M'},\quad \text{(C3)}$$

and write

$$\sum_J \sigma^\mu_J(\omega) = 4\pi\alpha \sum_{m',n,\mathbf{k},s} (\epsilon_{nk s} - \epsilon_C) \langle n, \mathbf{k}, s | r_\mu | \ell', m' \rangle \langle \ell', m' | r_\mu | n, \mathbf{k}, s \rangle \delta(\hbar\omega - \epsilon_{nk s} + \epsilon_C)$$

$$= 4\pi\alpha\hbar\omega \sum_{m',n,\mathbf{k},s} \langle n, \mathbf{k}, s | r_\mu | \ell', m' \rangle \langle \ell', m' | r_\mu | n, \mathbf{k}, s \rangle \delta(\hbar\omega - \epsilon_{nk s} + \epsilon_C).\quad \text{(C4)}$$

Now, we can rewrite the Kohn-Sham eigenfunctions using the PAW method. For our purposes, we can remain at the partial wave contribution. We therefore have

$$\sum_J \sigma^\mu_J(\omega) = 4\pi\alpha\hbar\omega \sum_{\substack{m',n,\mathbf{k},s \\ p_1,\ell_1,p_2,\ell_2,m_1,m_2}} \langle p_1, \ell_1, m_1 | r_\mu | \ell', m' \rangle \langle \ell', m' | r_\mu | p_2, \ell_2, m_2 \rangle P^{*n,\mathbf{k},s}_{p_1,\ell_1,m_1} P^{n,\mathbf{k},s}_{p_2,\ell_2,m_2} \delta(\hbar\omega - \epsilon_{nk s} + \epsilon_C).\quad \text{(C5)}$$

Writing $r_\mu = r\sqrt{\frac{4\pi}{3}} Y^\mu_1$, one can show that

$$\langle p_1, \ell_1, m_1 | r_\mu | \ell', m' \rangle = -(p_1, \ell_1 | r | \ell') C^{\ell',0}_{\ell_1,0,1,0} C^{\ell_1,m_1}_{1,\mu,\ell',m'},\quad \text{(C6)}$$

where the $(p_1, \ell_1 | r | \ell')$ are the radial integrations introduced in Eq. (8). This leads to

$$\sum_J \sigma^\mu_J(\omega) = 4\pi\alpha\hbar\omega \sum_{\substack{m',n,\mathbf{k},s \\ p_1,p_2,\ell_1,\ell_2,m_1,m_2}} (p_1, \ell_1 | r | \ell')(\ell' | r | p_2, \ell_2) C^{\ell',0}_{\ell_1,0,1,0} C^{\ell',0}_{\ell_2,0,1,0} C^{\ell_1,m_1}_{1,\mu,\ell',m'} C^{\ell_2,m_2}_{1,\mu,\ell',m'} P^{*n,\mathbf{k},s}_{p_1,\ell_1,m_1} P^{n,\mathbf{k},s}_{p_2,\ell_2,m_2} \delta(\hbar\omega - \epsilon_{nk s} + \epsilon_C).$$
$$\text{(C7)}$$

We will now sum over all the polarization directions μ and use the orthogonality relations from Eq. (C3),

$$\sigma(\omega) = \sum_\mu \sum_J \sigma^\mu_J(\omega) = 4\pi\alpha\hbar\omega \sum_{\substack{\mu,m',n,\mathbf{k},s \\ p_1,\ell_1,p_2,\ell_2,m_1,m_2}} (p_1, \ell_1 | r | \ell')(\ell' | r | p_2, \ell_2) C^{\ell',0}_{\ell_1,0,1,0} C^{\ell',0}_{\ell_2,0,1,0} C^{\ell_1,m_1}_{1,\mu,\ell',m'} C^{\ell_2,m_2}_{1,\mu,\ell',m'}$$

$$\times P^{*n,\mathbf{k},s}_{p_1,\ell_1,m_1} P^{n,\mathbf{k},s}_{p_2,\ell_2,m_2} \delta(\hbar\omega - \epsilon_{nk s} + \epsilon_C)$$

$$= 4\pi\alpha\hbar\omega \sum_{\substack{n,\mathbf{k},s \\ p_1,p_2,\ell_1,m_1}} (p_1, \ell_1 | r | \ell')(\ell' | r | p_2, \ell_2) \left(C^{\ell_1,0}_{\ell',0,1,0}\right)^2 P^{*n,\mathbf{k},s}_{p_1,\ell_1,m_1} P^{n,\mathbf{k},s}_{p_2,\ell_1,m_1} \delta(\hbar\omega - \epsilon_{nk s} + \epsilon_C).\quad \text{(C8)}$$

Splitting the two allowed dipole transitions $\ell_1 = \ell' \pm 1$, and neglecting the overlap between different projectors, we can rewrite this as

$$\sigma(\omega) \approx 4\pi\alpha\hbar\omega\left[\left|(\ell'+1|r|\ell')C^{\ell',0}_{\ell'+1,0,1,0}\right|^2\rho_{\ell'+1}(\omega+\epsilon_C/\hbar) + \left|(\ell'-1|r|\ell')C^{\ell'-1,0}_{\ell',0,1,0}\right|^2\rho_{\ell'-1}(\omega+\epsilon_C/\hbar)\right]$$

$$= 4\pi\alpha\hbar(\omega'-\epsilon_C/\hbar)\left[\frac{\ell'+1}{2\ell'+3}|(\ell'+1|r|l')|^2\rho_{\ell'+1}(\omega') + \frac{\ell'}{2\ell'-1}|(\ell'-1|r|\ell')|^2\rho_{\ell'-1}(\omega')\right]$$

$$= A_{\ell'}(\omega')\rho_{\ell'+1}(\omega') + B_{\ell'}(\omega')\rho_{\ell'-1}(\omega'), \qquad (C9)$$

where we introduced the ℓ partial densities of states ρ_ℓ and the shifted frequencies $\omega' = \omega + \epsilon_C/\hbar$. Therefore, the normalized edge $\sigma(\omega)$ can be written as a weighted sum of the partial densities of states corresponding to the dipole allowed ℓ values.

[1] P. Gutlich, Y. Garcia, and H. Goodwin, Chem. Soc. Rev. **29**, 419 (2000).

[2] J. A. Real, A. B. Gaspar, V. Niel, and M. C. Menoz, Coord. Chem. Rev. **236**, 121 (2003).

[3] H. Hao, X. H. Zheng, L. L. Song, R. N. Wang, and Z. Zeng, Phys. Rev. Lett. **108**, 017202 (2012).

[4] A. Bousseksou, G. Molnár, J. P. Tuchagues, N. Menéndez, E. Codjovi, and F. Varret, C. R. Chimie **6**, 329 (2003).

[5] J. Jeftic and A. Hauser, J. Phys. Chem. B **101**, 10262 (1997).

[6] V. Ksenofontov, A. B. Gaspar, G. Levchenko, B. Fitzsimmons, and P. Gutlich, J. Phys. Chem. B **108**, 7723 (2004).

[7] K. Tarafder, S. Kanungo, P. M. Oppeneer, and T. Saha-Dasgupta, Phys. Rev. Lett. **109**, 077203 (2012).

[8] D. J. Rudd, C. R. Goldsmith, A. P. Cole, T. D. P. Stack, K. O. Hodgson, and B. Hedman, Inorg. Chem. **44**, 1221 (2005).

[9] V. Briois, C. C. dit Moulin, P. Sainctavit, C. Brouder, and A.-M. Flank, J. Am. Chem. Soc. **117**, 1019 (1995).

[10] J.-J. Lee, H.-s. Sheu, C.-R. Lee, J.-M. Chen, J.-F. Lee, C.-C. Wang, C.-H. Huang, and Y. Wang, J. Am. Chem. Soc. **122**, 5742 (2000).

[11] R. K. Hocking, E. C. Wasinger, F. M. F. de Groot, K. O. Hodgson, B. Hedman, and E. I. Solomon, J. Am. Chem. Soc. **128**, 10442 (2006).

[12] T. Miyamachi, M. Gruber, V. Davesne, M. Bowen, S. Boukari, L. Joly, F. Scheurer, G. Rogez, T. K. Yamada, P. Ohresser *et al.*, Nat. Commun. **3**, 938 (2012).

[13] M. Gruber, A. Weismann, and R. Berndt, J. Phys. Condensed Matter **30**, 424001 (2018).

[14] R. Pasquier, K. Rassoul, and M. Alouani, Comput. Condens. Matter **32**, e00735 (2022).

[15] J. C. Slater, Adv. Quantum Chem. **6**, 1 (1972).

[16] J. C. Slater and K. H. Johnson, Phys. Rev. B **5**, 844 (1972).

[17] Note that strictly speaking the e_g and t_{2g} states form a symmetry adapted linear combination for the perfect octahedron as they form the basis set for the irreducible representations of the octahedron point group for the d states. As the symmetry is lowered, for example by a Janh-Teller distortions, a new symmetry adapted combination will be in principle more appropriate. Here the bond lengths and bond angles are slightly changed from those of the pristine octahedron and all five d states levels are split. We have found it practical to keep using the parent e_g and t_2g basis in order to see how the perturbative distortion affects the splittings of the now symmetry broken e_g and t_{2g} energy levels.

[18] P. E. Blöchl, Phys. Rev. B **50**, 17953 (1994).

[19] G. Kresse and J. Hafner, Phys. Rev. B **47**, 558 (1993).

[20] G. Kresse and J. Hafner, Phys. Rev. B **49**, 14251 (1994).

[21] G. Kresse and J. Furthmüller, Comput. Mater. Sci. **6**, 15 (1996).

[22] G. Kresse and J. Furthmüller, Phys. Rev. B **54**, 11169 (1996).

[23] G. Kresse and D. Joubert, Phys. Rev. B **59**, 1758 (1999).

[24] J. P. Perdew, K. Burke, and M. Ernzerhof, Phys. Rev. Lett. **77**, 3865 (1996).

[25] S. Grimme, J. Comput. Chem. **27**, 1787 (2006).

[26] A. I. Liechtenstein, V. I. Anisimov, and J. Zaanen, Phys. Rev. B **52**, R5467(R) (1995).

[27] S. L. Dudarev, G. A. Botton, S. Y. Savrasov, C. J. Humphreys, and A. P. Sutton, Phys. Rev. B **57**, 1505 (1998).

[28] S. Gueddida and M. Alouani, Phys. Rev. B **87**, 144413 (2013).

[29] P. A. M. Dirac and N. H. D. Bohr, Proc. Roy. Soc. London Ser. A **114**, 243 (1927).

[30] P. Sainctavit, M.-A. Arrio, and C. Brouder, Phys. Rev. B **52**, 12766 (1995).

[31] F. Karsai, M. Humer, E. Flage-Larsen, P. Blaha, and G. Kresse, Phys. Rev. B **98**, 235205 (2018).

[32] H. Ramanantoanina and M. Gruden, Int. J. Quantum Chem. **120**, e26081 (2020).

[33] A. Dixit and M. Alouani, Comput. Phys. Commun. **207**, 136 (2016).

[34] O. Bunău and M. Calandra, Phys. Rev. B **87**, 205105 (2013).

[35] P. A. M. Dirac and R. H. Fowler, Proc. Roy. Soc. London Ser. A **117**, 610 (1928).

[36] M. Taillefumier, D. Cabaret, A.-M. Flank, and F. Mauri, Phys. Rev. B **66**, 195107 (2002).

[37] D. D. Koelling and B. N. Harmon, J. Phys. C **10**, 3107 (1977).

[38] J. J. Sakurai and J. Napolitano, *Modern Quantum Mechanics* (Cambridge University Press, Cambridge, 2020), 3rd ed.

[39] A. R. Edmonds, *Angular Momentum in Quantum Mechanics* (Princeton University Press, Princeton, 2016).

[40] L. Grave de Peralta, Sci. Rep. **10**, 14925 (2020).

[41] M. Altarelli, Il Nuovo Cimento D **20**, 1067 (1998).

[42] B. T. Thole, P. Carra, F. Sette, and G. van der Laan, Phys. Rev. Lett. **68**, 1943 (1992).

[43] P. Carra, B. T. Thole, M. Altarelli, and X. Wang, Phys. Rev. Lett. **70**, 694 (1993).

[44] See Supplemental Material at http://link.aps.org/supplemental/10.1103/PhysRevB.108.094423, where we have shown the details of the number of electrons, magnetic moments of the octahedron nitrogen atoms, the iron density of states for various configuration of the FeN$_6$ configurations, as well as the iron $L_{2,3}$ edges for the ideal and distorted FeN$_6$ octahedron.

[45] C. Cartier dit Moulin, P. Rudolf, A. M. Flank, and C. T. Chen, J. Phys. Chem. **96**, 6196 (1992).

[46] J. Vinson, J. J. Rehr, J. J. Kas, and E. L. Shirley, Phys. Rev. B **83**, 115106 (2011).

[47] R. Laskowski and P. Blaha, Phys. Rev. B **82**, 205104 (2010).

[48] J. Schwitalla and H. Ebert, Phys. Rev. Lett. **80**, 4586 (1998).

[49] J.-P. Crocombette, B. T. Thole, and F. Jollet, J. Phys.: Condens. Matter **8**, 4095 (1996).

[50] R. Wu and A. J. Freeman, Phys. Rev. Lett. **73**, 1994 (1994).

[51] V. Jeanne-Rose and B. Poumellec, J. Phys.: Condens. Matter **11**, 1123 (1999).

[52] P. H. Schönemann and R. M. Carroll, Psychometrika **35**, 245 (1970).

[53] G. A. Rooke, J. Res. Natl. Bur. Stand. A Phys. Chem. **74A**, 273 (1970).